In Vivo Pulsatility Measurement of Cerebral Microcirculation in Rodents Using Dynamic Ultrasound Localization Microscopy

Chloé Bourquin, *Graduate Student Member, IEEE*, Jonathan Porée, *Member, IEEE*, Frédéric Lesage, and Jean Provost, *Member, IEEE*

***Abstract*— An increased pulse pressure, due to arteries stiffening with age and cardiovascular disease, may lead to downstream brain damage in microvessels and cognitive decline. Brain-wide imaging of the pulsatility propagation from main feeding arteries to capillaries in small animals could improve our understanding of the link between pulsatility and cognitive decline. However, it requires higher spatiotemporal resolution and penetration depth than currently available with existing brain imaging techniques. Herein, we show the feasibility of performing Dynamic Ultrasound Localization Microscopy (DULM), a novel imaging approach to capture hemodynamics with a subwavelength resolution. By producing cine-loops of flowing microbubbles in 2D in the whole rodent brain lasting several cardiac cycles, DULM performed pulsatility measurements in microvessels in-depth, in vivo, with and without craniotomy. Cortical veins and arteries were shown to have a significatively different pulsatility index and the method was compared against Contrast Enhanced Ultrafast Ultrasound Doppler (CEUFD) pulsatility measurements.**

***Index Terms*— Non-invasive in-depth transcranial brain imaging, cerebral microvascular pulsatile flow, pulsatility index, microbubbles, dynamic ultrasound localization microscopy.**

Manuscript received July 28, 2021; revised October 8, 2021; accepted October 19, 2021. Date of publication October 28, 2021; date of current version April 1, 2022. This work was supported in part by the Institute for Data Valorization (IVADO), in part by the Canada Foundation for Innovation under Grant 38095, and in part by the New Frontiers in Research Fund under Grant NFRFE-2018-01312. The work of Chloé Bourquin and Jonathan Porée was supported in part by IVADO, in part by the TransMedTech Institute, in part by the Fonds de recherche du Québec—Nature et technologies, in part by the Quebec Bio-Imaging Network, and in part by the Canada First Research Excellence Fund (Apogée/CFREF). *(Corresponding author: Jean Provost.)*

This work involved human subjects or animals in its research. Approval of all ethical and experimental procedures and protocols was granted by the Animal Care Ethics Committee of the Montreal Heart Institute under Permit Nos. 2019-2464 and 2018-32-03.

Chloé Bourquin and Jonathan Porée are with the Department of Engineering Physics, Polytechnique Montréal, Montréal, QC H3T 1J4, Canada (e-mail: chloe.bourquin@polymtl.ca; jonathan.poree@polymtl.ca).

Frédéric Lesage is with the Department of Electrical Engineering, Polytechnique Montréal, Montréal, QC H3T 1J4, Canada, and also with the Montreal Heart Institute, Montréal, QC H1T 1C8, Canada (e-mail: frederic.lesage@polymtl.ca).

Jean Provost is with the Department of Engineering Physics, Polytechnique Montréal, Montréal, QC H3T 1J4, Canada, and also with the Montreal Heart Institute, Montréal, QC H1T 1C8, Canada (e-mail: jean.provost@polymtl.ca).

This article has supplementary downloadable material available at https://doi.org/10.1109/TMI.2021.3123912, provided by the authors.

Digital Object Identifier 10.1109/TMI.2021.3123912

I. Introduction

LARGE arteries, such as the aorta and the carotids, are rich in elastic fibers at a young age, which dampens the downstream pulsatility, i.e., the fluctuations in blood velocity within the cardiac cycle. Their elasticity ensures a constant tissue perfusion in smaller arteries and arterioles [1]. Arterial stiffening develops with age [2], resulting in an excessive energy transmitted by the pulsatile flow [3] and the propagation of pulse pressure deeper into the brain [4], [5]. This excessive pulsatility impacts microvessels downstream, leading to an impaired regulation of the local blood flow [6], damage in capillaries and tissue, and finally cognitive decline [7], [8]. Studying this domino effect of the increase in pulsatility in the vascular tree could improve our understanding of its propagation, its evolution, and its role in neurodegenerative diseases. It would require however a measure of pulsatility in the whole brain, from large vessels to capillaries.

Brain pulsatility measurements are commonly performed at single locations of the vascular tree as an indirect measure of the whole brain pulsatility: upstream in large arteries with Transcranial Doppler ultrasonography (TCD) [9], [10] and Magnetic Resonance Imaging (MRI) [11], or downstream in capillaries at the brain surface with optical microscopy [12], [13]. Pulsatility of blood flow can be quantified with a pulsatility index (PI) [14], which reflects the variations of the blood flow velocity compared to its mean velocity; but it can also be characterized by the velocity waveform itself, which presents a pulsatile pattern synchronized with the cardiac rhythm for a high pulsatility [15].

To perform a whole-brain measurement, Ultrafast Ultrasound Doppler (UFD) [16] imaging can be used to measure rapid blood flow fluctuations in large vessels [17]. The smaller vessels anatomy can also be mapped [18], [19], but typically at the cost of a reduced temporal resolution. Moreover, the velocity resolution of its Pulsed-Wave (PW) Doppler spectra is bound to the wavelength and the pulse repetition frequency, leading to an incontrovertible trade-off [20] between temporal, spatial and velocity resolutions. This trade-off prevents the measure of pulsatility in microvessels throughout the small animal brain.

Recently, a novel technique called Ultrasound Localization Microscopy (ULM) [21], [22] has been developed to map

microvessels in entire brain cross-sections in rats with a ~10-μm resolution using a 15 MHz linear array [23]. Based on the subwavelength localization and tracking of microbubbles, it requires several minutes [24] to reconstruct a map of the entire vascular tree and its averaged velocity. It has been used recently to measure velocity maxima and minima to provide hemodynamic parameters in the human brain [25], but this technique has never been used to measure the pulsatility, which requires to sample the velocity fluctuations within at least one cardiac cycle.

Herein, we introduce Dynamic Ultrasound Localization Microscopy (DULM), which enables pulsatility measurements in 2D in the rodent brain in vivo, with and without craniotomy. More specifically, we measured the pulsatility with DULM in microvessels (i.e., smaller than 100 μm in diameter) in a rat brain with craniotomy and in a mouse brain through skull and skin. We compared DULM against Contrast Enhanced Ultrafast Ultrasound Doppler (CEUFD) spectra. We finally separated veins and arteries in the cortex using microbubbles flow direction and verified that cortical veins and arteries had a significatively different pulsatility index (PI). These results indicate that DULM can produce highly resolved dynamic maps of the blood flow and provides a novel method to better understand the pulsatility propagation at-depth, by performing for the first time non-invasive pulsatility measurements deep in the brain.

II. Methods

A. Ethics

This study was carried out in accordance with the recommendations of the guide for the care and use of laboratory animals of the Canadian Council for Animal Care. All procedures were approved by the Animal Care Ethics Committee of the Montreal Heart Institute (Permit Number: 2019-2464, 2018-32-03).

B. Rat Preparation for Ultrasound Imaging With Craniotomy

The surgery and ultrasound acquisitions in a female adult rat were performed under 2 % isoflurane anesthesia while body temperature was maintained at 35°C with a small animal monitoring platform (Labeo Technologies Inc., QC, Canada). The head of the animal was placed in a stereotaxic frame to limit motion, and the skull was removed following craniotomy to limit aberrations using a surgical micro drill, yielding a $\sim$ 15 mm $\times$ 10 mm window over the brain. The ultrasound acquisitions were started after an intravenous bolus injection in the jugular vein, lasting 30-60 seconds, of a 50-μL microbubble solution (1.2×10^{10} microbubbles per milliliter, Definity, Lantheus Medical Imaging, MA, USA) diluted in 50 μL of saline, followed by a saline flush, with a 27G needle.

C. Mouse Preparation for Ultrasound Imaging Through Skull and Skin

The preparation and ultrasound acquisitions in a male adult mouse were performed under 2 % isoflurane anesthesia while body temperature was maintained at 35°C with a small animal monitoring platform (Labeo Technologies Inc., QC, Canada). Excess hair on the mouse's skin was removed with hair removal cream Veet (Reckitt Benckiser, Poland). The head of the animal was placed in a stereotaxic frame to limit motion. The ultrasound acquisitions were launched after an intravenous bolus injection in the tail vein, lasting 30-60 seconds, of a 25-μL microbubble solution (1.2×10^{10} microbubbles per milliliter, Definity, Lantheus Medical Imaging, MA, USA) diluted in 25 μL of saline, followed by a saline flush, with a 30G needle.

D. Ultrafast Ultrasound Acquisitions

Vital parameters (electrocardiogram (ECG), breathing frequency, temperature) were recorded simultaneously by the monitoring platform during the acquisitions. Acoustic coupling was ensured by centrifuged ultrasound gel. In vivo rodent brains were imaged at 15 MHz with a 128-element linear array probe with a pitch of 100 μm (Vermon, Tours, France). The probe was connected to a programmable ultrafast ultrasound system (Vantage 256, Verasonics, WA, USA). 800 groups of 400 frames were acquired during 10 minutes at a 1000-Hz frame rate (Fig. 1), using 3 tilted plane waves ($-1°$, $0°$, $1°$) at a depth of 12 mm. Each group was gated on the R-wave of the ECG recorded using the monitoring platform.

E. Beamforming and Tissue Signal Cancelation

Algorithms were implemented using MATLAB (R2019a, The MathWorks, Inc., Natick, MA). First, beamforming was performed on channel data (Fig. 2) and compounded (3 angles), to reconstruct 800 groups of 400 IQ frames on a 23.5 μm $\times$ 23.5 μm cartesian grid using an in-house GPU implementation of the delay-and-sum beamformer. The IQ frames were then normalized by the square root of the number of channel contributions per pixel [26]. Then, tissue signal removal was performed by applying a Singular Value Decomposition (SVD) [27] filter and setting the first 10 singular values to zero. This cutoff corresponds to a compromise between suppressing tissue and keeping both fast and slow microbubbles.

F. ULM Processing

To prevent false detection of diffuse scattering arising from the interaction of multiple microbubbles, filtered IQ frames were first correlated with the spatial impulse response (or Point Spread Function, PSF) of the imaging system (Fig. 2). To simulate the PSF, we used an in-house GPU implementation of the SIMUS simulation software described in [28], using the probe parameters and the acquisition sequence. After correlation, local maxima were detected in the resulting correlation map and identified as unique microbubbles, and their subpixel positions were calculated using a 2D Gaussian least square fitting using a 7-pixels neighborhood. Due to the bolus injection performed at the beginning of the acquisition, the microbubbles concentration decreased through time: to prevent false microbubbles detection, bright local maxima

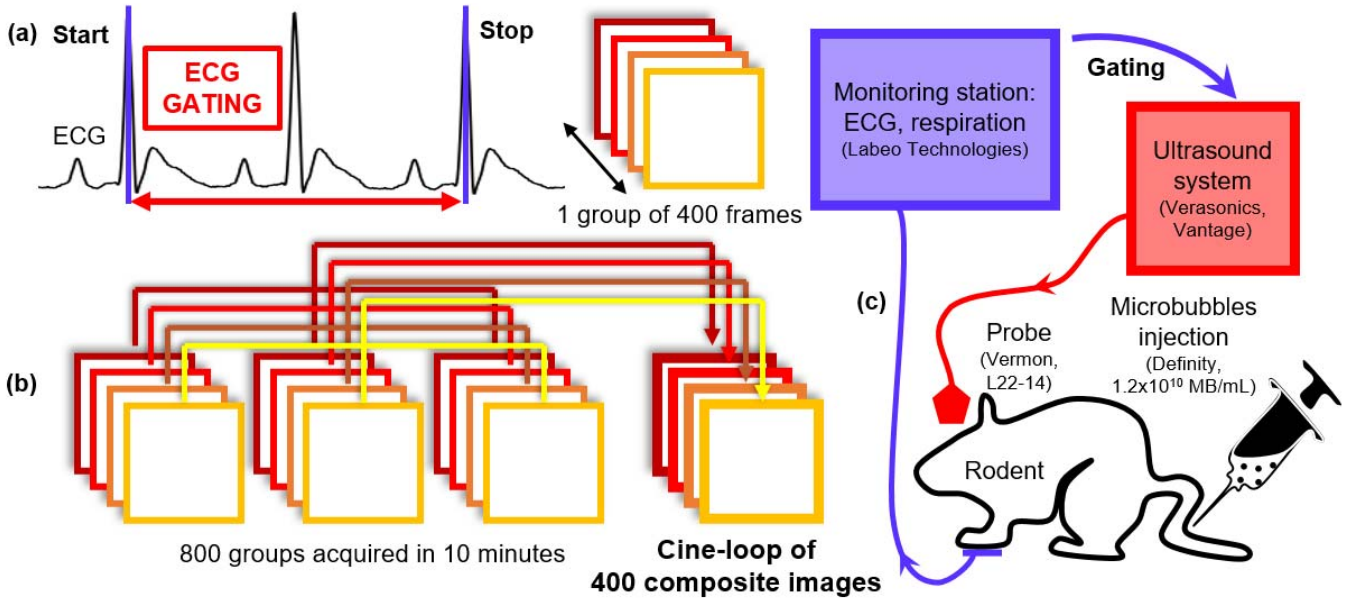

Fig. 1. DULM sequence design. After a single bolus injection of a microbubbles solution, 800 groups of 400 frames @1000 Hz were acquired, over a period of 10 minutes. Each group was gated on the R-wave of the ECG (a) using a synchronization trigger between the monitoring station and the ultrasound system (c). The groups were then post-processed and combined together (b) to obtain a cine-loop of 400 composite images of the whole brain cross-section.

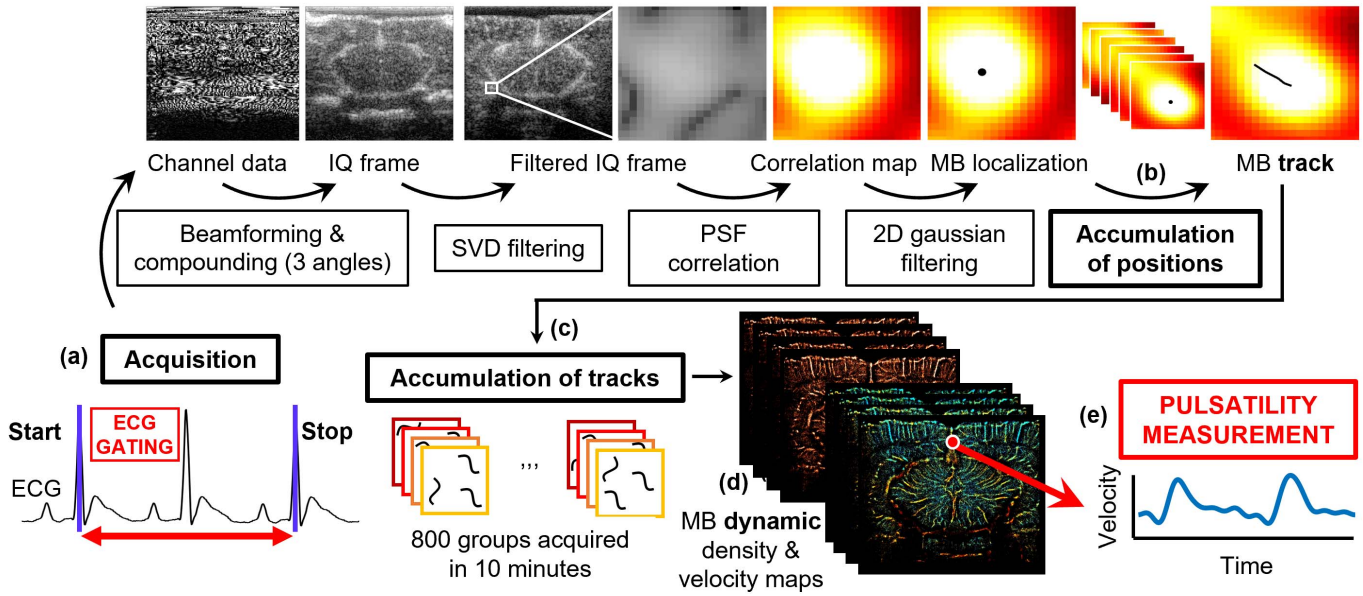

Fig. 2. DULM pipeline (see Methods). The post-processing pipeline was applied as follows: after beamforming and compounding (3 angles), the In-Phase & Quadrature (IQ) frames were filtered using a Singular Value Decomposition (SVD) filter to remove the tissue while keeping the MB signal. A Point Spread Function (PSF) correlation was then applied to generate a correlation map, on which MB could be localized using a 2D Gaussian filter. (b) The accumulation of the MB positions in successive frames over time led to an ensemble of tracks. (c) After generating all the tracks, the sum of microbbubles positions and their averaged velocity allowed to generate (d) MB dynamic density and velocity maps. (e) From these maps, the pulsatility could be measured in any vessel in the whole brain cross-section. MB: microbubbles.

with a correlation coefficient lower than 0.4 were rejected. Microbubbles were then paired as tracks with the nearest neighbor method in the following frame (Fig. 2 (b)).

G. DULM Processing

After tracking, the velocity of hundreds of thousands of microbubbles over the hundreds of cardiac cycles that occurred during the 10-minutes acquisition was computed. Since each group of 400 frames at 1000 Hz was gated on the R-wave of the ECG signal, corresponding to a recording of 400 ms (Fig. 1), these velocities were then averaged (Fig. 2 (c)) to retrieve a mean velocity variation through time, lasting 400 ms (Fig. 2(d)). This method provides measurements that are calculated on a blood velocity waveform retrieved from the accumulation of hundreds of cardiac cycles.

This 400-ms sequence corresponds to the duration of about 2 cardiac cycles in the rat brain (its heart rate was approximately 300 bpm), and 3.6 in the mouse brain (its heart rate was approximately 550 bpm).

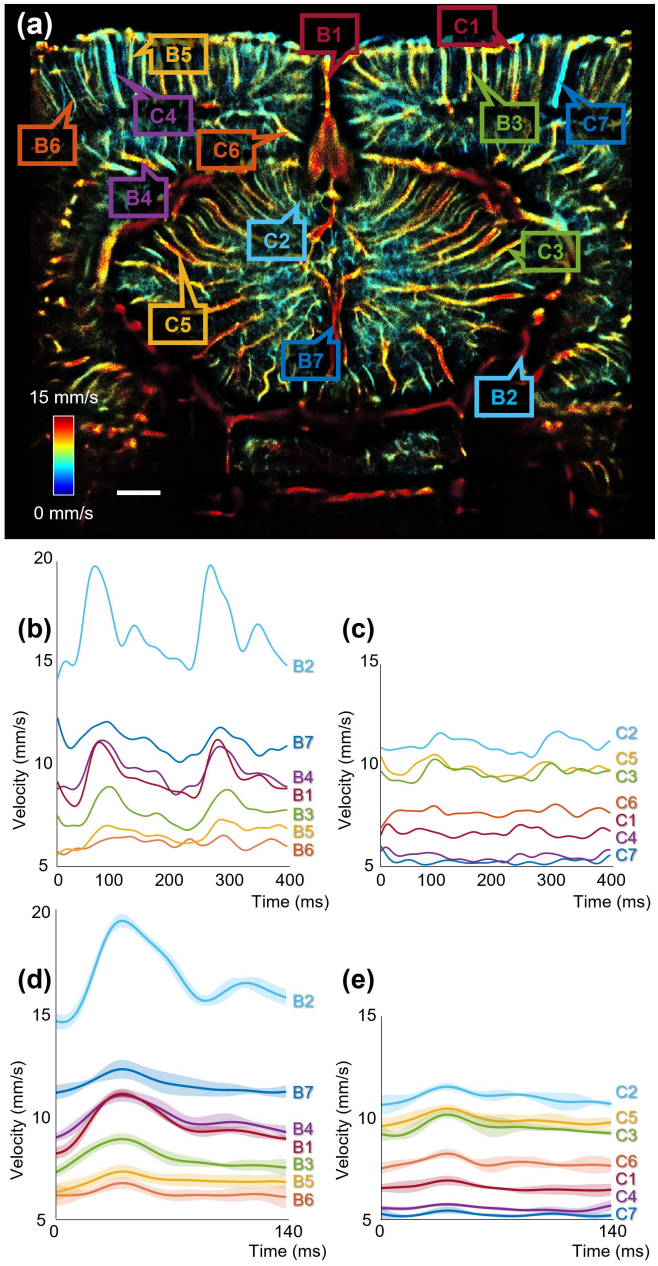

Fig. 3. Pulsatility measurements performed by DULM in 14 vessels selected in the rat brain with craniotomy. (a) Mean velocity map. (b-c) Velocity variations over time (400 ms) of vessels with a high (B1-B7) and a low (C1-C7) pulsatility. (d-e) Average velocity waveform over time for vessels with a high (B1-B7) and a low (C1-C7) pulsatility after dividing the dataset into 4 sets of 200 groups of frames. Shaded regions: mean $\pm$ standard deviation ($4 \leq N \leq 8$ velocity waveforms). Grid resolution for the maps: 10 μm $\times$ 10 μm. Scale bars, 1 mm.

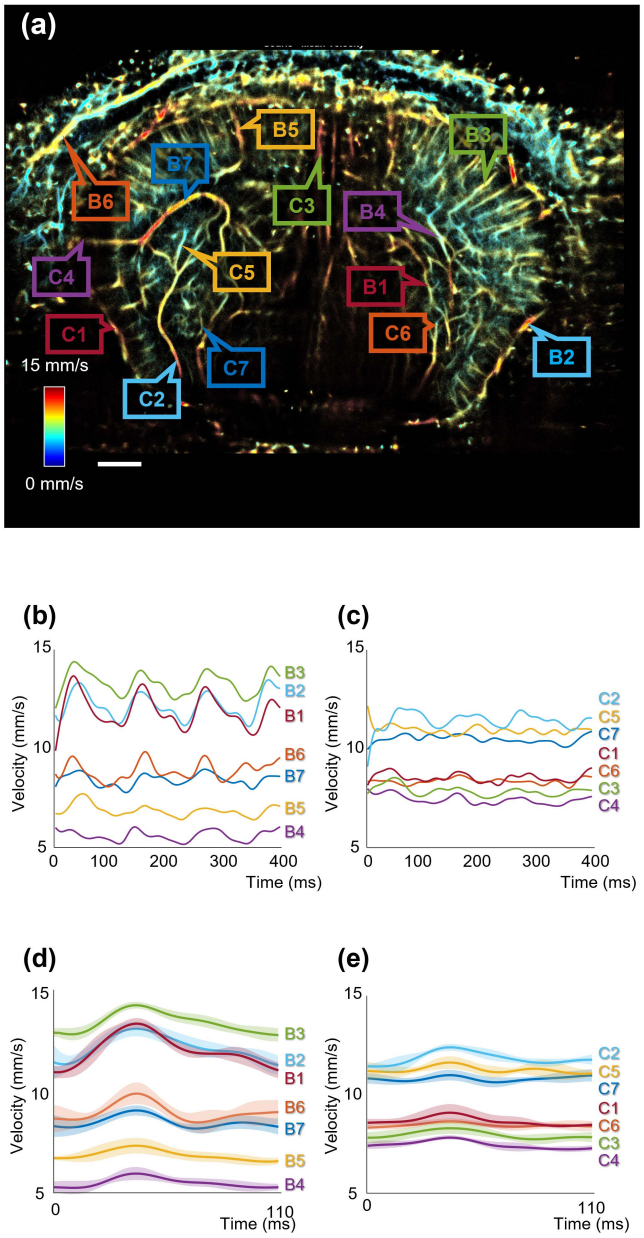

Fig. 4. Pulsatility measurements performed by DULM in 14 vessels selected in the mouse brain through skull and skin. (a) Mean velocity map. (b-c) Velocity variations over time (400 ms) of vessels with a high (B1-B7) and a low (C1-C7) pulsatility. (d-e) Average velocity waveform over time for vessels with a high (B1-B7) and a low (C1-C7) pulsatility, after dividing the dataset into 2 sets of 400 groups of frames. Shaded regions: mean $\pm$ standard deviation ($4 \leq N \leq 8$ velocity waveforms). Grid resolution for the maps: 10 μm $\times$ 10 μm. Scale bars, 1 mm.

Microbubbles positions were summed and their velocities were averaged on a finer cartesian grid (10 μm $\times$ 10 μm) according to their timing within the 400-ms recording. By doing so, we obtained both microbubbles density and velocity dynamic maps lasting 2 and 3.6 cardiac cycles, in the rat and the mouse brains, respectively.

H. Dynamic Density and Velocity Maps

Dynamic density and velocity maps were further processed as videos (e.g., Supplementary videos 1 and 2). For a better visualization, a 4-frame sliding temporal window was applied and a representative ECG signal was added to indicate the elapsed time after gating. Static maps were displayed next to the dynamic ones, as a reference.

I. Pulsatility Measurement in a Vessel

In each 10 μm $\times$ 10 μm pixel, all the microbubbles (positions and velocities) extracted from the 800 groups were accumulated over a common 400-ms temporal axis, to extract the evolution of the microbubbles velocity over time within this pixel (Fig. 2 (e)). Vessels were manually segmented

to accumulate several pixels and average the evolution of thousands of microbubble velocities. Missing values were replaced by the median value of the signal. High frequencies in the velocity signal were filtered out (butter 3rd order, 25-Hz cutoff), which was sufficient to sample the cardiac cycles of both species and observe the velocity fluctuations over 400 ms (Fig. 3 (b-c) and Fig. 4 (b-c)).

J. Pulsatility Index (PI) Calculation

The PI is usually calculated from the envelope of a Pulsed-Wave Doppler spectrum: it is defined in (1) as the difference between the peak systolic velocity (PSV) and the end diastolic velocity (EDV), divided by the mean flow velocity (MFV):

$$PI = \frac{PSV - EDV}{MFV} \tag{1}$$

A mean PI is usually calculated over several complete velocity waveforms (typically between 4 and 6), to avoid biased measurements due to irregularities in the spectrum.

Similarly, to assess the repeatability of DULM, we divided our datasets to perform a PI measurement based on several velocity waveforms. After calculating velocity variations in each vessel (Fig. 3 (b-c) and Fig. 4 (b-c)), we kept portions of velocity waveforms that were part of a complete heart cycle to compute an average velocity waveform (Fig 3 (d-e) and Fig 4 (d-e)). Since the sequence we used allowed to record only 1 or 2 complete velocity waveforms in the rat brain (and 3 in the mouse brain), we divided our dataset into 4 $\times$ 200 frames for the rat and 2 $\times$ 400 frames for the mouse, to ensure an accurate measurement of the PI and assess it reproducibility. Thus, each PI measurement was performed on at least 4 velocity waveforms, and a maximum of 8.

After measuring the maximum (PSV_i), minimum (EDV_i) and mean velocity (MFV_i) and calculating a PI_i for each velocity waveform i ($i = 1, \ldots, N$ with $4 \leq N \leq 8$), we computed the average PI and standard deviation σ_{PI}:

$$PI = \frac{1}{N}\sum_{i=1}^{N} PI_i = \frac{1}{N}\sum_{i=1}^{N} \frac{PSV_i - EDV_i}{MFV_i} \tag{2}$$

$$\sigma_{PI} = \sqrt{\frac{1}{N-1}\sum_{i=1}^{N} |PI_i - PI|^2} \tag{3}$$

This standard deviation calculation was used to assess the reproducibility of the PI measurements from one velocity waveform to the other.

K. Vessel Diameter Estimation

The vessel diameters were estimated from the microbubbles mean density maps generated by DULM: by evaluating the number of microbubbles across the section of the selected vessel, the full width at half maximum was considered as the vessel diameter.

L. Flow Direction, Pulsatility and Statistical Analysis in the Cortex

A Fast Fourier Transform filter [29] was applied on the channel data, to separate the microbubbles according to their flowing direction (upwards and downwards) (Fig. 5 (a) and Fig. 6 (a)). After the DULM post-processing pipeline, we manually segmented the cortex (Fig. 5 (b) and Fig. 6 (b)): there, veins flow upwards and arteries flow downwards. A vessel segmentation was then performed by applying a Hessian filter on the mean density map (Fig. 5 (c-d) and 6 (c-d)). For each pixel found within a segmented vessel, we extracted the average velocity variations and calculated the PI as described above. We considered that the more microbubbles had been flowing through this pixel, the more accurate this PI measurement would be. This is why we attributed a weight to each pixel, corresponding to the microbubble density of this pixel. The statistical comparison between veins and arteries was then performed using a weighted Student's t-test, which takes the pixels weights into account to determine whether the two groups of pixels (veins and arteries) have equal means. The weights were also considered to calculate the weighted median, 25th and 75th percentile of each group, to display the weighted boxplots (Fig. 5 (e) and Fig. 6 (e)).

M. Contrast Enhanced Ultrafast Ultrasound Doppler (CEUFD)

A CEUFD pipeline was implemented by summing the channel data of all the groups of the acquisition, to enhance the signal-to-noise ratio. By doing so, we could get a 400-frames dataset with a very high composite concentration of microbubbles (Fig. 7 (a) and Fig. 8 (a)), to compute CEUFD spectra and perform measurements similar to CEUS (Contrast Enhanced Ultrasound) acquisitions [30], [31]. With the parameters we used in the ultrasound sequences (a transmitted frequency of 15.625 MHz and a PRF of 1000 Hz), the maximum velocity that could be measured with CEUFD is 24.64 mm/s.

Beamforming was performed on the summed channel data, with a 23.5 μm $\times$ 23.5 μm cartesian grid using an in-house, GPU-based, delay-and-sum beamformer. SVD filtering was then applied, with the first 10 singular values set to zero. In selected vessels, the spectrum was computed within regions of interest (ROI) of 3 pixels $\times$ 3 pixels (70 μm $\times$ 70 μm) (Fig. 7 (c) and Fig. 8 (c)): a spectrum was estimated by performing the average of the 9 individual spectra. Thus, for each temporal sample, we calculated the power spectral estimation by a Fast Fourier Transform over a temporal window of 27 ms, to obtain a gray-scaled column in the spectrogram [19]. The size of the temporal window was chosen to be short compared to the time scale of the cardiac cycle ($\sim$ 200 ms for the rat, $\sim$ 110 ms for the mouse), but long enough to enable a velocity estimation and draw a velocity waveform. By sliding the temporal window and iterating the calculation for each temporal sample, we finally obtained the spectrum of microbubbles velocity variations over time in each ROI (Fig. 7 (e) and Fig. 8 (e)). The envelope of the signal was computed from the binarization of the spectrum performed with the Otsu method [32], and frequencies higher than 25 Hz were filtered out. From this envelope, velocity minima and maxima were extracted, as well as the times they were reached.

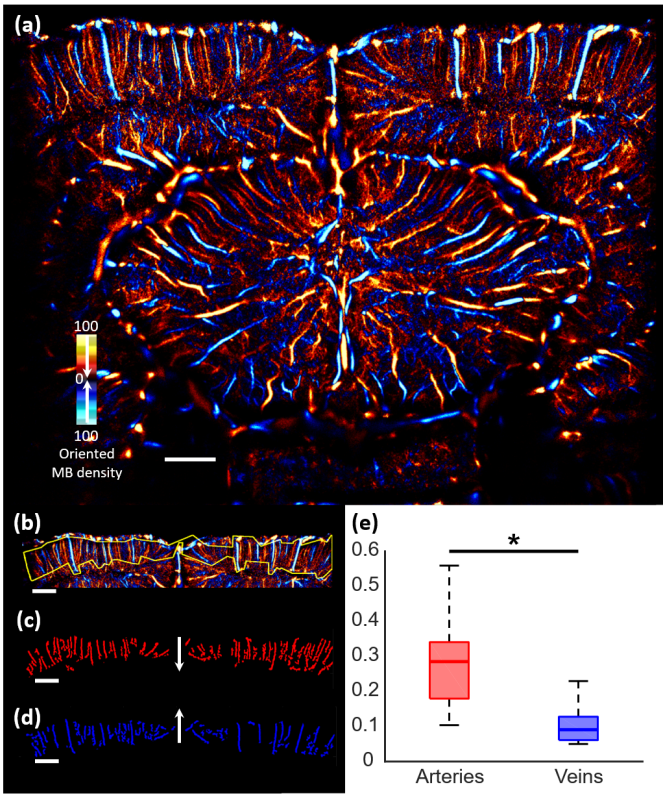

Fig. 5. DULM-based PI could differentiate veins from arteries in the rat cortex. (a) Oriented microbubbles (MB) density (hot: MB flowing downwards, cold: MB flowing upwards). (b) Manual segmentation of the cortex (yellow). (c-d) 69 veins (blue) and 82 arteries (red) were differentiated from their flow direction (veins flowing upwards, arteries flowing downwards). (e) Pulsatility indexes (PI) calculated in all the pixels contained in the segmented arteries (red box) and veins (blue box), weighted by their MB density: 23,737 PI values were extracted in the rat arteries, 18,125 in the rat veins. Weighted boxplot: thick line, weighted median; box, 25th to 75th weighted percentile; whiskers extend to the most extreme data points that are not considered outliers; outliers (0 for the rat arteries, 1,149 for the rat veins) are not represented. *P $<$ 0.001. Scale bars, 1 mm.

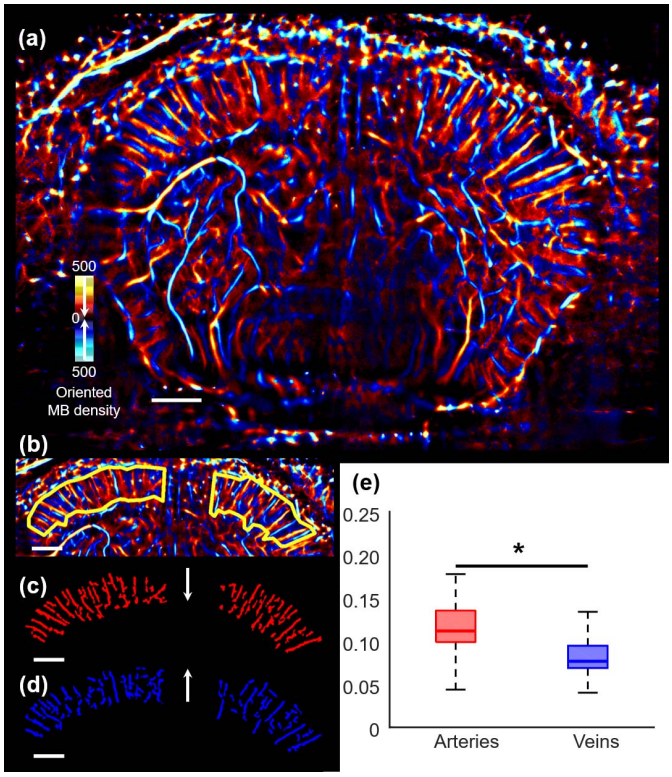

Fig. 6. DULM-based PI could differentiate veins from arteries in the mouse cortex. (a) Oriented microbubbles (MB) density (hot: MB flowing downwards, cold: MB flowing upwards). (b) Manual segmentation of the cortex (yellow). (c-d) 62 veins (blue) and 57 arteries (red) were differentiated from their flow direction (veins flowing upwards, arteries flowing downwards). (e) Pulsatility indexes (PI) calculated in all the pixels contained in the segmented arteries (red box) and veins (blue box), weighted by their MB density: 19,160 PI values were extracted in the mouse arteries, 18,394 in the mouse veins. Weighted boxplot: thick line, weighted median; box, 25th to 75th weighted percentile; whiskers extend to the most extreme data points that are not considered outliers; outliers (1,390 for the mouse arteries, 2,379 for the mouse veins) are not represented. *P $<$ 0.001. Scale bars, 1 mm.

III. Results

A. DULM Enables the Extraction of Flow Variations Over Time and Spatially Resolved Whole-Brain Pulsatility Measurements in 2D in Microvessels

The dynamic maps generated by DULM (Supplementary videos 1 and 2) show microbubbles flowing in the bloodstream in the whole brain cross-section. The pulsatility can be observed on the video in some vessels shown by the arrows.

Vessels with different diameters and mean velocities were selected in both species (Fig. 3 (a) and Fig. 4 (a)) to obtain an overview of the performances of the method applied to different flow patterns: large and small vessels, fast and slow flow.

Blood flow pulsatility was quantified by calculating the pulsatility index, or PI [14] (Methods), which reflects the variations of the blood flow velocity compared to its mean velocity. The pulsatility can also be qualitatively characterized by the velocity waveform itself, which presents a pulsatile pattern synchronized with the cardiac rhythm for a high pulsatility [15]. We arbitrarily separated the vessels into two groups according to their PI with a threshold of PI $=$ 0.13 in the rat brain and PI $=$ 0.12 in the mouse brain, to better visualize the velocity waveform for a high (Fig. 3 (b) and Fig. 4 (b)) pulsatility, and for a low (Fig. 3 (c) and Fig. 4 (c)) pulsatility. The corresponding mean velocities, PI and vessel widths are listed in Table I and Table II.

In both animals, we observed that the pulsatile pattern is more visible in the variations of velocity over time for a high pulsatility, i.e. for a PI $>$ 0.13 in the rat brain and PI $>$ 0.12 in the mouse brain (Fig. 3 (b), B1: PI $=$ 0.33 $\pm$ 0.03 in the rat; Fig. 4 (b), B1: PI $=$ 0.22 $\pm$ 0.02 in the mouse); for a low pulsatility (PI $<$ 0.13 in the rat brain and PI $<$ 0.12 in the mouse brain), the variations of velocity though time present a flatter pulse and a less discernable pulsatile pattern (Fig. 3 (c), C7: PI $=$ 0.09 $\pm$ 0.03 in the rat; Fig. 4 (c), C7: PI $=$ 0.04 $\pm$ 0.03 in the mouse). The pulsatile pattern was observed even in presence of low velocities (Fig. 3 (b), B3: 7.7 $\pm$ 0.10 mm/s in the rat; Fig. 4 (b), B4: 5.6 $\pm$ 0.07 mm/s in the mouse) and in small vessels (Fig. 3 (b), B6: 27 $\pm$ 6 μm in the rat; Fig. 4 (b), B4: 26 $\pm$ 2 μm in the mouse).

TABLE I
PULSATILITY INDEX MEASUREMENTS PERFORMED BY DULM IN THE RAT BRAIN WITH CRANIOTOMY. SD: STANDARD DEVIATION

VESSEL	DIAMETER ± SD (μM)	MEAN VELOCITY ± SD (MM/S)	PULSATILITY INDEX ± SD
B1	36 ± 6	9.4 ± 0.03	0.33 ± 0.03
B2	122 ± 4	16.7 ± 0.04	0.30 ± 0.06
B3	64 ± 7	7.7 ± 0.10	0.28 ± 0.04
B4	72 ± 8	9.7 ± 0.12	0.24 ± 0.04
B5	45 ± 7	6.6 ± 0.20	0.21 ± 0.03
B6	27 ± 6	6.1 ± 0.29	0.18 ± 0.03
B7	47 ± 9	11.5 ± 0.12	0.13 ± 0.05
C1	46 ±7	6.5 ± 0.07	0.13 ± 0.03
C2	72 ± 5	11.0 ± 0.11	0.13 ± 0.09
C3	78 ± 11	9.5 ± 0.14	0.12 ± 0.06
C4	69 ± 12	5.4 ± 0.05	0.10 ± 0.03
C5	73 ± 9	9.8 ± 0.13	0.11 ± 0.04
C6	97 ± 9	7.7 ± 0.14	0.11 ± 0.02
C7	64 ± 7	5.1 ± 0.02	0.09 ± 0.03

TABLE II
PULSATILITY INDEX MEASUREMENTS PERFORMED BY DULM IN THE MOUSE BRAIN THROUGH SKULL AND SKIN. SD: STANDARD DEVIATION

VESSEL	DIAMETER ± SD (μM)	MEAN VELOCITY ± SD (MM/S)	PULSATILITY INDEX ± SD
B1	70 ± 6	12.3 ± 0.05	0.22 ± 0.02
B2	56 ± 7	12.5 ± 0.005	0.17 ± 0.02
B3	72 ± 5	13.7 ± 0.06	0.12 ± 0.02
B4	26 ± 2	5.6 ± 0.07	0.12 ± 0.04
B5	63 ± 11	6.9 ± 0.17	0.13 ± 0.02
B6	48 ± 6	9.1 ± 0.10	0.19 ± 0.04
B7	55 ± 6	8.6 ± 0.13	0.13 ± 0.02
C1	50 ±7	8.7 ± 0.10	0.08 ± 0.06
C2	66 ± 9	11.8 ± 0.05	0.09 ± 0.06
C3	98 ± 10	8.0 ± 0.05	0.08 ± 0.04
C4	60 ± 11	7.5 ± 0.13	0.07 ± 0.08
C5	75 ± 13	11.3 ± 0.12	0.08 ± 0.03
C6	71 ± 12	8.5 ± 0.07	0.06 ± 0.07
C7	65 ± 9	10.8 ± 0.12	0.04 ± 0.03

In Fig. 4 (d-e) and Fig. 5 (d-e), we noticed a high repeatability in the average velocity waveform, with a small standard deviation calculated from N independent measurements ($4 \leq N \leq 8$). Especially, for a high pulsatility (B1 and B2 in both animals), after the systolic peak, velocity waveforms present a local minimum before another increase in velocity. This minimum corresponds to a dicrotic notch, which can be seen usually in arteries: it is due to the sudden decrease in arterial pressure that occurs immediately after the closure of the aortic valves. This local velocity minimum is less or not visible in vessels with a smaller PI, in both animals.

B. Differentiating Cortical Veins From Arteries With DULM

Oriented microbubble density maps along with the segmented cortical veins (flowing upwards) and cortical arteries (flowing downwards) are shown in Fig. 5 and 6. In each segmented vessel, the PI was calculated. After weighting by the microbubbles density, a significatively higher pulsatility was observed in cortical arteries compared to cortical veins ($P < 0.001$), in both animals (Fig. 5 (e) and Fig. 6 (e)).

C. Comparison of CEUFD and DULM Pulsatility Measurement Performances

A comparison with another ultrasound method was performed as follows, in order to compare their performances in terms of extracting a pulsatility pattern in microvessels. Two different processing pipelines were applied on the same data of the rat and the mouse brains: the DULM pipeline on the one hand, and a CEUFD pipeline on the other hand (Methods). Indeed, like UFD [19], [33], CEUFD imaging can be used to image the microvascularisation of the small animal brain, with an enhanced contrast in the PW Doppler spectra due to the microbubbles signal. Different vessels were selected in the entire brain to compare the pulsatility measurements obtained with CEUFD (Fig. 7 (a) and Fig. 8 (a)) and DULM (Fig. 7 (b) and Fig. 8 (b)).

In both animals, a difference in the mean velocities between the two methods can be seen. This bias can be explained by the fact that CEUFD images are less resolved than DULM images: consequently, CEUFD measurements were performed in a 70 μm × 70 μm region, whereas DULM measurements were performed in a 30 μm × 30 μm region. Also, as a Doppler imaging technique, CEUFD is an angle-dependent method: the measured velocity depends on the angle between the ultrasound beam and the vessel. On the contrary, DULM velocity measurements are angle-independent and performed on the average velocity variations of thousands of microbubbles. Moreover, due to low contrast, it was difficult to extract velocity measurements in CEUFD. For these reasons, we qualitatively compared the two methods and focused on the velocity waveform instead of the velocity and PI measurements.

Also, it should be noted that DULM measures absolute velocity variations, whereas CEUFD measurements depends on flow direction: this is why the pattern is reversed in CEUFD for vessels 1 and 2 in the rat brain (Fig. 7 (e2-3)), and vessel 1 in the mouse brain (Fig. 8 (e1)).

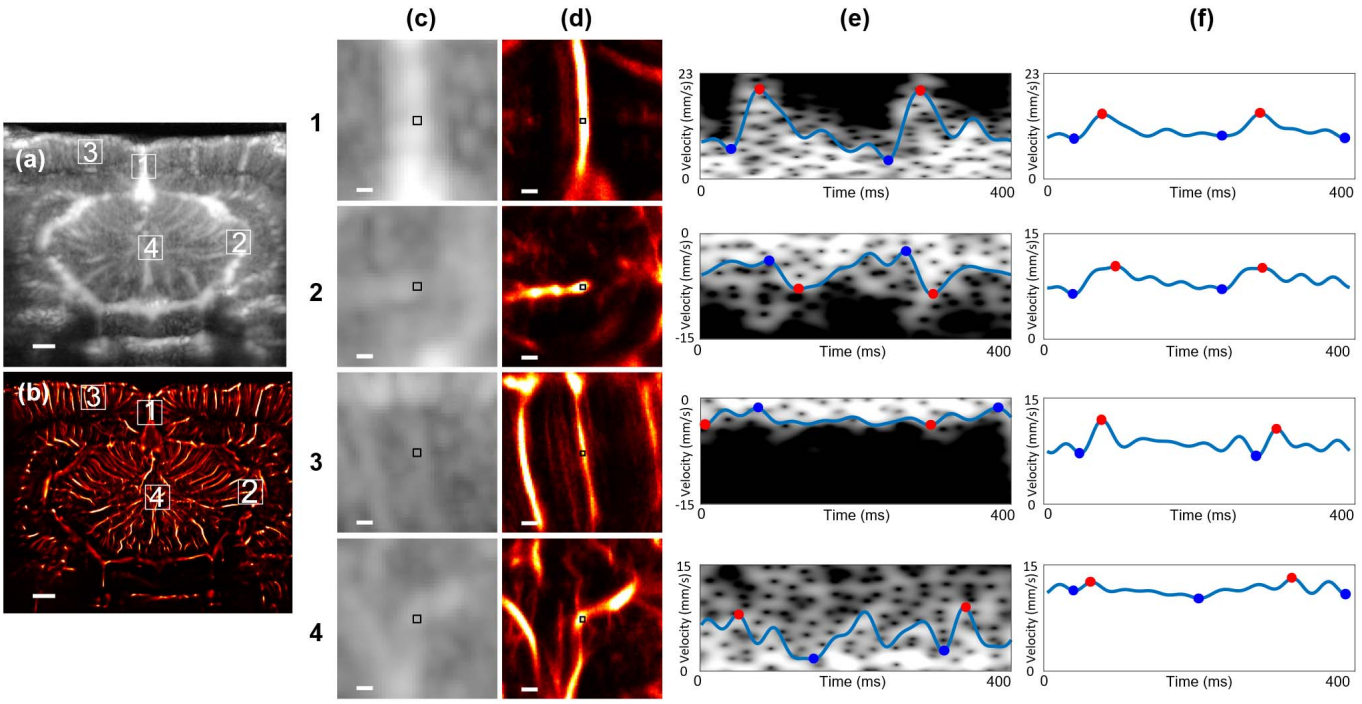

Fig. 7. Comparison of pulsatility measurements between CEUFD and DULM in the rat brain. Several vessels were selected in the whole brain to measure the pulsatility with both (a) CEUFD and (b) DULM. (c1-4) Closer view of each vessel with CEUFD. Regions where the pulsatility was measured within each vessel are 70 μm $\times$ 70 μm with CEUFD (black squares). (d1-4) Closer view of each selected vessel with DULM. Regions where the pulsatility was measured within each vessel are 30 μm $\times$ 30 μm with DULM (black squares). (e1-4) The CEUFD spectra envelopes show the velocity variations over time. (f1-4) Velocity variations though time obtained with DULM. For both methods, the velocity minima (blue spots) and maxima (red spots) were extracted. Grid resolution for the maps: 23.5 μm $\times$ 23.5 μm in CEUFD, 10 μm $\times$ 10 μm in DULM. Scale bars, (a&b) 1 mm, (c&d, 1-4) 100 μm.

In both animals, we found main vessels (labelled 1 in both figures) in which the pulsatility could be measured with CEUFD (Fig. 7 (e1) and Fig. 8 (e1)) and DULM (Fig. 7 (f1) and Fig. 8 (f1)): a pulsatile pattern synchronized with the cardiac rhythm was extracted from the velocity waveforms with both methods, in the rat brain and the mouse brain. Moreover, the times at which the velocity reached its maxima were found to be within an error of 17 $\pm$ 14 ms. In these vessels, nearly 10,000 microbubble events were detected in the 30 μm $\times$ 30 μm DULM ROI: 8,756 in the mouse brain (Fig. 8 (d1)) and 11,632 in the rat brain (Fig. 7 (d1)).

In vessel 2 in Fig. 7, fewer microbubble events (7,894, see Fig. 7 (d2)) were detected in the DULM ROI: we observed a non-reproductible pulse in CEUFD (Fig. 7 (e2)), but again a pulsatile pattern in DULM (Fig. 7 (f2)).

In vessels 3 in Fig. 7, and 2 and 3 in Fig. 8, it was found that the pulsatile pattern remained visible in DULM (Fig. 7 (f3), Fig. 8 (f2-3)), but could not be detected with CEUFD in the spectra (Fig. 7 (e3), Fig. 8 (e2-3)). In these vessels, even fewer microbubble events were detected in the DULM ROI: 3,381 in vessel 3 in the rat brain (Fig. 7 (d3)), and 6,109 in vessel 2 (Fig. 8 (d2)) and 4,053 in vessel 3 (Fig. 8 (d3)) in the mouse brain.

Finally, a non-pulsatile flow was observed using DULM in vessel 4 in Fig. 7(f4), but could not be detected using CEUFD (Fig. 7 (e4)). In this vessel, 4,211 microbubble events were detected in the DULM ROI.

IV. Discussion

In this study, Dynamic Ultrasound Localization Microscopy (DULM) was used to image the blood velocity as a function of time and measure pulsatility indices in rat and mouse brains, with and without craniotomy (through skull and skin), respectively. More specifically, DULM was used to produce cine-loops of flowing microbubbles in the entire brain and lasting several cardiac cycles. From these cine-loops, density and velocity dynamic maps of flowing microbubbles were extracted, as well as the evolution of the velocity over time in vessels smaller than 100 μm in diameter, from which the pulsatility index (PI) was calculated. The velocity over time obtained with DULM was compared against CEUFD. DULM detected a significatively higher PI in the cortical arteries than in the cortical veins.

Supplementary videos 1 and 2 illustrate that DULM can be used to generate density and velocity dynamic maps of flowing microbubbles in the entire rodent brain. In Fig. 3 and Fig. 4, velocity variations over time and PI calculations were extracted for 14 different vessels in the whole rodent brain cross-section, and a pulsatile pattern synchronized with the cardiac rhythm of the animal could be recognized in the velocity waveforms for a high pulsatility, even for slow flow and small vessels. To assess reproducibility, a mean PI and an average velocity waveform were calculated from $4 \leq N \leq 8$ independent measurements performed in each vessel, with a small standard deviation.

As expected [34], Fig. 5 and Fig. 6 showed that after identification based on flow direction in the cortex, arteries

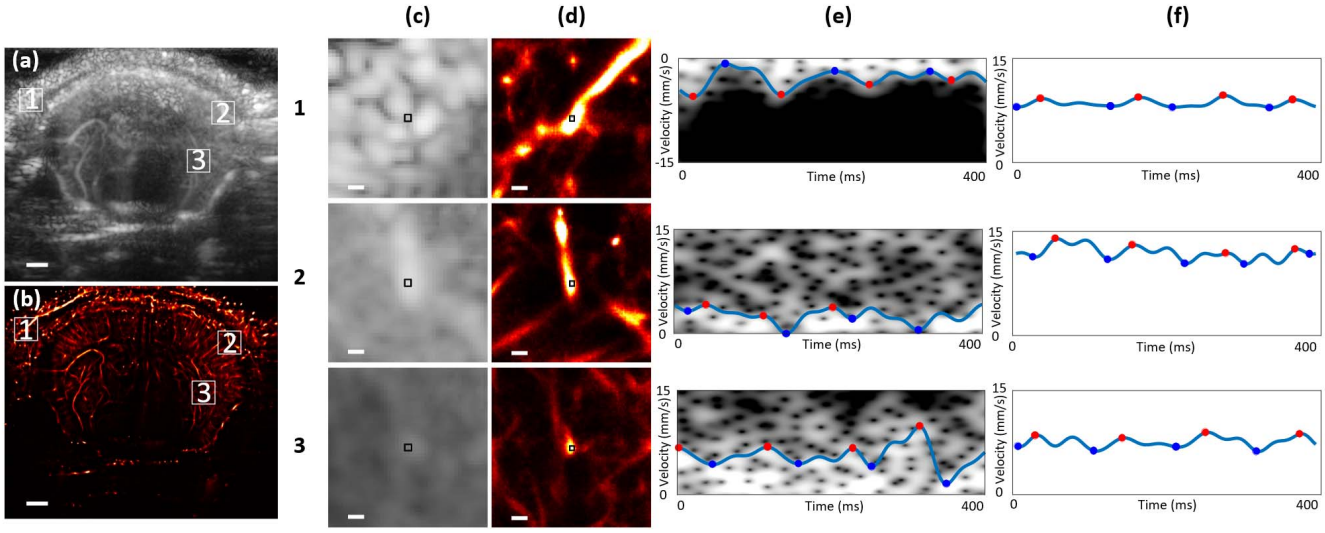

Fig. 8. Comparison of pulsatility measurements between CEUFD and DULM in the mouse brain. Several vessels were selected in the whole brain to measure the pulsatility with both (a) CEUFD and (b) DULM. (c1-3) Closer view of each vessel with CEUFD. Regions where the pulsatility was measured within each vessel are 70 μm $\times$ 70 μm with CEUFD (black squares). (d 1-3) Closer view of each selected vessel with DULM. Regions where the pulsatility was measured within each vessel are 30 μm $\times$ 30 μm with DULM (black squares). (e1-3) The CEUFD spectra envelopes show the velocity variations over time. (f1-3) Velocity variations though time obtained with DULM. For both methods, the velocity minima (blue spots) and maxima (red spots) were extracted. Grid resolution for the maps: 23.5 μm $\times$ 23.5 μm in CEUFD, 10 μm $\times$ 10 μm in DULM. Scale bars, (a&b) 1 mm, (c&d, 1-3) 100 μm.

(flowing downwards) had a significatively higher PI than the veins (flowing upwards). Fig. 7 and Fig. 8 illustrated that using the same datasets to compare the two modalities, velocity waveforms based on DULM were better defined and allowed for the probing of more microvessels than CEUFD, which could measure the pulsatility only in main vessels where many microbubbles had flown.

DULM could potentially impact current pre-clinical practices. Indeed, a DULM acquisition could provide 1) microbubbles density and velocity dynamic maps in the whole rodent brain cross-section; 2) the velocity variations over time in microvessels; 3) the calculation of the PI within this vessel. Until now, the PI was calculated within larger regions of interest, in large arteries such as the carotid or main vessels in the brain. With DULM, we achieved a high spatiotemporal resolution, and extracted the pulsatility in both large and small vessels, at-depth, in the whole brain vasculature in 2D. This technique provides dynamic measurements in a new range of vessels that was inaccessible for non-invasive techniques before: it could be used to study the propagation of the pulsatility along the vascular tree the case of aging arteries, to better enhance its impact deep in the brain.

The study presented herein is however not without limitations. In this work, we limited our measurement to the average pulsatility in entire cross-sections of blood vessels. In principle, different pulsatility values could be obtained within one vessel.

Since no method has been able to perform 2D whole-brain measurements of the pulsatility in small animals in vivo before, it is difficult to compare these results with the literature. However, in vivo measurements performed in the cortex are common in small animals. Average velocity measurements performed in the mouse cortical vessels with a diameter of 72 $\pm$ 5 μm (Fig. 4 (b), B3: 13.7 $\pm$ 0.06 mm/s) and a diameter of 63 $\pm$ 11 μm (Fig. 4 (b), B5: 6.9 $\pm$ 0.17 mm/s) agree with two-photon excited fluorescence microscopy measurements [35], which report a mean velocity of 13 mm/s in arterioles with a 60-μm diameter. Similarly, velocity variations observed in the rat cortex for a 64 $\pm$ 7 μm diameter (Fig. 3 (b), B3: 7.7 $\pm$ 0.10 mm/s) between 6.9 mm/s and 8.9 mm/s agree with velocity variations observed in pial arterioles (6-12 mm/s) with optical coherence tomography [36] for a vessel with a 62.4-μm diameter.

It is also difficult to quantitatively establish the smallest vessel diameter in which pulsatility can be measured as PI measurements depend on both the resolution of ULM at high concentration and the value of the PI itself. Indeed, while a clear pulsatility pattern was extracted in many micovessels from the velocity waveforms, for some vessels the velocity modulation with the cardiac cycle was less visible. In veins for example, the pulsatility may be very low and undetectable with our method.

This study was based on the use of bolus injections rather than a constant infusion because bolus injections are simpler to perform, potentially minimize microbubbles destruction [37] and limit issues linked to dead volumes in catheters. However, bolus injections lead to a varying microbubble concentration during the acquisition, which may affect the variability of the velocity measurements. In order to partially lift this limitation, we used a 0.4 correlation threshold to reduce measurements with very high variability.

To sample the velocity variations over time, a large number of microbubbles have to be detected and tracked during the acquisition. To increase the number of microbubbles, a few solutions exist: increasing the acquisition time, and/or increasing the concentration of injected microbubbles. Here, about 6 times more microbubbles were injected, compared to other ULM studies in the rat brain [24] (see Methods), and the

acquisition times reached approximately 10 minutes. However, the number of injected microbubbles remains low compared to Contrast Enhanced Ultrasound [31], where the microbubbles are not detected individually. The drawback of injecting more microbubbles is that the localization of the microbubbles is more difficult due to multiple microbubble interactions, and can lead to a degraded resolution. A complete study of the influence of microbubbles concentration on the reconstructed vessels is the object of on-going work [38], [39].

The comparison between CEUFD and DULM was provided as an illustrative example and based on an acquisition sequence designed for DULM, which means that better CEUFD images could probably be obtained by optimizing imaging parameters such as frame rate and the number of compounding angles. It is however unlikely it would change the general results obtained in this work, i.e., that DULM provides improved velocity measurements in the microvasculature at the cost of a longer acquisition time.

Another limitation of DULM is that just like ULM, it cannot yet be converted into a real-time technique: it requires an acquisition of a few minutes in order to detect enough microbubbles to reconstruct vessels and measure their pulsatility. Additionally, it should be noted that here we did not correct for the aberrations due to the skull in the mouse, inducing a duplication of some vessels in-depth, and we did not perform any motion correction, which could affect the pulsatility measurements. Corrections for aberration [25] and motion [40] are the subject of on-going research [41] and could in principle be applied for DULM at the cost of increased computational time.

V. Conclusion

In conclusion, Dynamic Ultrasound Localization Microscopy is a novel approach for obtaining dynamic information about small vessels in-depth in the whole brain. Such a technology allows for the mapping of microbubbles flow in entire 2D fields of view. It also promises to overcome the current limitations of brain imaging techniques, and to generate a host of novel 2D applications ranging from brain vascularization dynamic mapping (with or without craniotomy) to the measurement of novel biomarkers.

Acknowledgment

The authors would like to thank M.-A. Gillis for the surgery, and M. Abran and S. Belanger for technical help with the monitoring platform.

References

[1] D. Barić, "Why pulsatility still matters: A review of current knowledge," *Croatian Med. J.*, vol. 55, no. 6, pp. 609–620, Dec. 2014, doi: 10.3325/cmj.2014.55.609.

[2] E. G. Lakatta, M. Wang, and S. S. Najjar, "Arterial aging and subclinical arterial disease are fundamentally intertwined at macroscopic and molecular levels," *Med. Clinics North Amer.*, vol. 93, no. 3, pp. 583–604, May 2009, doi: 10.1016/j.mcna.2009.02.008.

[3] N. Thorin-Trescases and E. Thorin, "Lifelong cyclic mechanical strain promotes large elastic artery stiffening: Increased pulse pressure and old age-related organ failure," *Can. J. Cardiol.*, vol. 32, no. 5, pp. 624–633, May 2016, doi: 10.1016/j.cjca.2015.12.022.

[4] P. Maillard *et al.*, "Aortic stiffness, increased white matter free water, and altered microstructural integrity: A continuum of injury," *Stroke*, vol. 48, no. 6, pp. 1567–1573, Jun. 2017, doi: 10.1161/STROKEAHA.116.016321.

[5] M. F. O'Rourke and J. Hashimoto, "Mechanical factors in arterial aging: A clinical perspective," *J. Amer. College Cardiol.*, vol. 50, no. 1, pp. 1–13, Jul. 2007, doi: 10.1016/j.jacc.2006.12.050.

[6] G. F. Mitchell, "Effects of central arterial aging on the structure and function of the peripheral vasculature: Implications for end-organ damage," *J. Appl. Physiol.*, vol. 105, no. 5, pp. 1652–1660, 2008, doi: 10.1152/japplphysiol.90549.2008.

[7] G. F. Mitchell, "Aortic stiffness, pressure and flow pulsatility, and target organ damage," *J. Appl. Physiol.*, vol. 125, no. 6, pp. 1871–1880, Dec. 2018, doi: 10.1152/japplphysiol.00108.2018.

[8] M. P. Pase, A. Herbert, N. A. Grima, A. Pipingas, and M. F. O'Rourke, "Arterial stiffness as a cause of cognitive decline and dementia: A systematic review and meta-analysis," *Internal Med. J.*, vol. 42, no. 7, pp. 808–815, Jul. 2012, doi: 10.1111/j.1445-5994.2011.02645.x.

[9] E.-Y. Lim, D.-W. Yang, A.-H. Cho, and Y. S. Shim, "Cerebrovascular hemodynamics on transcranial Doppler ultrasonography and cognitive decline in mild cognitive impairment," *J. Alzheimer's Disease*, vol. 65, no. 2, pp. 651–657, Jan. 2018, doi: 10.3233/JAD-180026.

[10] R. Aaslid, T.-M. Markwalder, and H. Nornes, "Noninvasive transcranial Doppler ultrasound recording of flow velocity in basal cerebral arteries," *J. Neurosurgery*, vol. 57, no. 6, pp. 769–774, Dec. 1982, doi: 10.3171/jns.1982.57.6.0769.

[11] M. Holmgren, A. Wåhlin, T. Dunås, J. Malm, and A. Eklund, "Assessment of cerebral blood flow pulsatility and cerebral arterial compliance with 4D flow MRI," *J. Magn. Reson. Imag.*, vol. 51, no. 5, pp. 1516–1525, May 2020, doi: 10.1002/jmri.26978.

[12] E. Guevara, N. Sadekova, H. Girouard, and F. Lesage, "Optical imaging of resting-state functional connectivity in a novel arterial stiffness model," *Biomed. Opt. Exp.*, vol. 4, no. 11, pp. 2332–2346, Oct. 2013, doi: 10.1364/BOE.4.002332.

[13] O. De Montgolfier *et al.*, "High systolic blood pressure induces cerebral microvascular endothelial dysfunction, neurovascular unit damage, and cognitive decline in mice," *Hypertension*, vol. 73, no. 1, pp. 217–228, Jan. 2019, doi: 10.1161/HYPERTENSIONAHA.118.12048.

[14] R. G. Gosling and D. H. King, "Arterial assessment by Doppler-shift ultrasound," *Proc. Roy. Soc. Med.*, vol. 67, no. 6 Pt 1, pp. 447–449, Jun. 1974.

[15] W. I. Rosenblum, "Erythrocyte velocity and a velocity pulse in minute blood vessels on the surface of the mouse brain," *Circulat. Res.*, vol. 24, no. 6, pp. 887–892, Jun. 1969, doi: 10.1161/01.res.24.6.887.

[16] M. Tanter and M. Fink, "Ultrafast imaging in biomedical ultrasound," *IEEE Trans. Ultrason., Ferroelectr., Freq. Control*, vol. 61, no. 1, pp. 102–119, Jan. 2014, doi: 10.1109/TUFFC.2014.6689779.

[17] J. Bercoff *et al.*, "Ultrafast compound Doppler imaging: Providing full blood flow characterization," *IEEE Trans. Ultrason., Ferroelectr., Freq. Control*, vol. 58, no. 1, pp. 134–147, Jan. 2011, doi: 10.1109/TUFFC.2011.1780.

[18] E. Macé, G. Montaldo, I. Cohen, M. Baulac, M. Fink, and M. Tanter, "Functional ultrasound imaging of the brain," *Nature Methods*, vol. 8, no. 8, pp. 662–664, Aug. 2011, doi: 10.1038/nmeth.1641.

[19] C. Demené *et al.*, "Ultrafast Doppler reveals the mapping of cerebral vascular resistivity in neonates," *J. Cereb. Blood Flow Metab.*, vol. 34, no. 6, pp. 1009–1017, Jun. 2014, doi: 10.1038/jcbfm.2014.49.

[20] *Comprehensive Biomedical Physics*. Accessed: Jul. 21, 2021. [Online]. Available: https://www.elsevier.com/books/comprehensive-biomedical-physics/brahme/978-0-444-53632-7

[21] O. Couture, V. Hingot, B. Heiles, P. Muleki-Seya, and M. Tanter, "Ultrasound localization microscopy and super-resolution: A state of the art," *IEEE Trans. Ultrason., Ferroelectr., Freq. Control*, vol. 65, no. 8, pp. 1304–1320, Aug. 2018, doi: 10.1109/TUFFC.2018.2850811.

[22] K. Christensen-Jeffries *et al.*, "Super-resolution ultrasound imaging," *Ultrasound Med. Biol.*, vol. 46, no. 4, pp. 865–891, Apr. 2020, doi: 10.1016/j.ultrasmedbio.2019.11.013.

[23] C. Errico *et al.*, "Ultrafast ultrasound localization microscopy for deep super-resolution vascular imaging," *Nature*, vol. 527, no. 7579, pp. 499–502, Nov. 2015, doi: 10.1038/nature16066.

[24] V. Hingot, C. Errico, B. Heiles, L. Rahal, M. Tanter, and O. Couture, "Microvascular flow dictates the compromise between spatial resolution and acquisition time in ultrasound localization microscopy," *Sci. Rep.*, vol. 9, no. 1, Dec. 2019, Art. no. 2456, doi: 10.1038/s41598-018-38349-x.

[25] C. Demené *et al.*, "Transcranial ultrafast ultrasound localization microscopy of brain vasculature in patients," *Nature Biomed. Eng.*, vol. 5, no. 3, pp. 219–228, Mar. 2021, doi: 10.1038/s41551-021-00697-x.

[26] B. Berthon *et al.*, "Spatiotemporal matrix image formation for programmable ultrasound scanners," *Phys. Med. Biol.*, vol. 63, no. 3, 2018, Art. no. 03NT03, doi: 10.1088/1361-6560/aaa606.

[27] C. Demené *et al.*, "Spatiotemporal clutter filtering of ultrafast ultrasound data highly increases Doppler and fUltrasound sensitivity," *IEEE Trans. Med. Imag.*, vol. 34, no. 11, pp. 2271–2285, Nov. 2015, doi: 10.1109/TMI.2015.2428634.

[28] S. Shahriari and D. Garcia, "Meshfree simulations of ultrasound vector flow imaging using smoothed particle hydrodynamics," *Phys. Med. Biol.*, vol. 63, no. 20, Oct. 2018, Art. no. 205011, doi: 10.1088/1361-6560/aae3c3.

[29] B.-F. Osmanski, M. Pernot, G. Montaldo, A. Bel, E. Messas, and M. Tanter, "Ultrafast Doppler imaging of blood flow dynamics in the myocardium," *IEEE Trans. Med. Imag.*, vol. 31, no. 8, pp. 1661–1668, Aug. 2012, doi: 10.1109/TMI.2012.2203316.

[30] C. Greis, "Quantitative evaluation of microvascular blood flow by contrast-enhanced ultrasound (CEUS)," *Clin. Hemorheol. Microcirculat.*, vol. 49, nos. 1–4, pp. 137–149, Jan. 2011, doi: 10.3233/CH-2011-1464.

[31] D. Premilovac, S. J. Blackwood, C. J. Ramsay, M. A. Keske, D. W. Howells, and B. A. Sutherland, "Transcranial contrast-enhanced ultrasound in the rat brain reveals substantial hyperperfusion acutely post-stroke," *J. Cerebral Blood Flow Metabolism*, vol. 40, no. 5, pp. 939–953, May 2020, doi: 10.1177/0271678X20905493.

[32] N. Otsu, "A threshold selection method from gray-level histograms," *IEEE Trans. Syst., Man, Cybern.*, vol. SMC-9, no. 1, pp. 62–66, Jan. 1979, doi: 10.1109/TSMC.1979.4310076.

[33] B.-F. Osmanski, E. Lecarpentier, G. Montaldo, V. Tsatsaris, P. Chavatte-Palmer, and M. Tanter, "Discriminative imaging of maternal and fetal blood flow within the placenta using ultrafast ultrasound," *Sci. Rep.*, vol. 5, no. 1, Sep. 2015, Art. no. 13394, doi: 10.1038/srep13394.

[34] M. E. Wagshul, P. K. Eide, and J. R. Madsen, "The pulsating brain: A review of experimental and clinical studies of intracranial pulsatility," *Fluids Barriers CNS*, vol. 8, no. 1, p. 5, Jan. 2011, doi: 10.1186/2045-8118-8-5.

[35] T. P. Santisakultarm *et al.*, "*In vivo* two-photon excited fluorescence microscopy reveals cardiac- and respiration-dependent pulsatile blood flow in cortical blood vessels in mice," *Amer. J. Physiol.-Heart Circulat. Physiol.*, vol. 302, no. 7, pp. H1367–H1377, Apr. 2012, doi: 10.1152/ajpheart.00417.2011.

[36] J. Seki, Y. Satomura, Y. Ooi, T. Yanagida, and A. et Seiyama, "Velocity profiles in the rat cerebral microvessels measured by optical coherence tomography," *Clin. Hemorheol. Microcirculat.*, vol. 34, nos. 1–2, pp. 233–239, Jan. 2006.

[37] C. Sun *et al.*, "Influence of temperature, needle gauge and injection rate on the size distribution, concentration and acoustic responses of ultrasound contrast agents at high frequency," *Ultrasonics*, vol. 70, pp. 84–91, Aug. 2016, doi: 10.1016/j.ultras.2016.04.013.

[38] H. Belgharbi *et al.*, "An anatomically and hemodynamically realistic simulation framework for 3D ultrasound localization microscopy," Oct. 2021, doi: 10.1101/2021.10.08.463259.

[39] L. Milecki *et al.*, "A deep learning framework for spatiotemporal ultrasound localization microscopy," *IEEE Trans. Med. Imag.*, vol. 40, no. 5, pp. 1428–1437, May 2021, doi: 10.1109/TMI.2021.3056951.

[40] V. Hingot, C. Errico, M. Tanter, and O. Couture, "Subwavelength motion-correction for ultrafast ultrasound localization microscopy," *Ultrasonics*, vol. 77, pp. 17–21, May 2017.

[41] P. Cormier, J. Poree, C. Bourquin, and J. Provost, "Dynamic myocardial ultrasound localization angiography," *IEEE Trans. Med. Imag.*, Jun. 2021, doi: 10.1109/TMI.2021.3086115.